Dynamics-driven tailoring of sub-nanometric Pt-Ni bimetals confined in hierarchical zeolite for catalytic hydrodeoxygenation

Yajie Tian [a,*], Longhui Guo [a], Congzhen Qiao [a], Zixu Sun [b,*], Yusuke Yamauchi [c,d,**], Shude Liu [c,e,**]

[a] Henan Engineering Research Center of Functional Materials and Catalytic Reaction, Green Energy and Materials International Joint Lab, College of Chemistry and Molecular Sciences, Henan University, Kaifeng 475004, China
[b] Key Lab for Special Functional Materials of Ministry of Education, School of Materials Science and Engineering, Henan University, Kaifeng 475004, China
[c] Department of Materials Process Engineering, Graduate School of Engineering, Nagoya University, Nagoya 464–8603, Japan
[d] School of Chemical Engineering and Australian Institute for Bioengineering and Nanotechnology, University of Queensland, Brisbane, QLD 4072, Australia
[e] College of Textiles, Donghua University, Shanghai 201620, China

ARTICLE INFO

ABSTRACT

Metal-zeolite catalysts are promising for hydrodeoxygenation of bio-oils, but they always encounter sluggish diffusion kinetics due to sole micropores and inferior metal stability. Here, highly stable sub-nanoscale Pt-Ni bimetals confined in a hierarchical ZSM-5 zeolite (Pt-Ni@HZ) are constructed. The formed Pt-Ni@HZ species create framework-bonding metal sites with zeolite in a confined microenvironment, thereby establishing strong interactions and generating uniform distribution of Pt-Ni bimetals. In the Pt-Ni@HZ-catalyzed hydrodeoxygenation of phenolics, sub-nanometric Pt-Ni facilitates the adsorption and transfer of hydrogen, and hierarchical pores promote the diffusion kinetics of reactants. The designed Pt-Ni@HZ with small metal particles and high coordination numbers of Pt-Ni bonds, favors the complete deoxygenation of phenolics, with a higher yield of cyclohexane than conventional catalysts prepared by impregnation. Benefiting from the protection of the zeolite framework, the Pt-Ni@HZ catalyst exhibits high thermal stability and low leaching of metal active sites, with only 4.4 % catalyst deactivation after five reaction cycles.

1. Introduction

Bio-oil has been identified as an alternative energy source to fossil fuels, which holds great potential [1,2]. However, the bio-oil produced by conventional pyrolysis and/or hydrothermal liquefaction of bio-mass has high oxygen content, leading to serious chemical instability and corrosivity, which thus requires upgrading [3–5]. Hydrodeoxygenation (HDO) has been considered a prominent way to eliminate oxygen atoms while preserving carbon atoms in products [6]. Bi-functional acid carrier supported metal catalysts are considered one of the most promising catalysts for hydrodeoxygenation (HDO) reactions in both liquid and vapor phases, as reported in several studies [7]. The HDO reaction can be essentially regulated through changing the interaction between metal and support. Metal active sites (Ni, Co, Pt, Pd, etc.) catalyze the hydrogenation of reactants [8]. Zeolites, which possess abundant acidities, high surface areas, and high hydrothermal stability, are considered

potential supports for deoxygenation [9,10]. While noble metals (such as Pt, Pd, and Au) exhibit superior HDO activity and stability, their use is economically unfeasible. In contrast, transition metals (such as Ni, Co, and Mo) are available at a lower cost but require relatively high loadings (usually above 5 %) to achieve the desired activity [11,12]. Recently, the use of supported bimetallic catalysts are deemed as an interesting concept to improve the catalytic performance [13]. Especially, the mixture of noble metals with transition metals can effectively modify the electronic and/or geometric factor to tailor the catalytic reactivity, selectivity and stability [14].

Generally, microporous zeolite-supported metal catalysts are obtained by ion exchange or impregnation. However, metal species are prone to aggregation during preparation and/or catalytic reactions, and this reduces the utilization of the metal active sites [15–18]. To address this, metal active centers have been often encapsulated in zeolites [19–22]. In this strategy, highly dispersed metal active sites are confined

---

* Corresponding authors.
** Corresponding authors at: Department of Materials Process Engineering, Graduate School of Engineering, Nagoya University, Nagoya 464–8603, Japan.
E-mail addresses: yjtian@henu.edu.cn (Y. Tian), sunzixu317@163.com (Z. Sun), y.yamauchi@uq.edu.au (Y. Yamauchi), sdliu@dhu.edu.cn (S. Liu).

in zeolite channels to establish metal-zeolite interactions [23,24]. To date, several strategies have focused on encapsulating uniform metal sites in zeolites; these strategies include one-pot (bottom-up) [25–27], post-treatment (top-down) [28–30], and in situ crystal transformation approaches [31–33]. However, the mere presence of micropores in these zeolites generally limits intragranular diffusion, resulting in low utilization of the active metal sites in catalytic reactions [34–36].

Hierarchically porous zeolites (HZs) encapsulating metal catalysts have been employed to improve the diffusion of reactants into zeolite catalysts with micropores only [37–41]. The active surface of the metal species becomes readily accessible through the spatial connection between the microporous and mesoporous channels, thus ensuring high catalytic activity [42,43]. However, the hierarchical pores in zeolites that can capture metal active sites commonly generate undesired framework defects, leading to poor thermal stability, and thus restricting their practical applications [41]. Recently, reducing the crystal sizes of zeolites with defect-free structures has been shown to hold great potential for addressing diffusion limitations [44]. Nanoscale zeolites with spatial diffusion paths (intercrystalline pores) connected with microporous channels effectively promote the conversion of macromolecules [45–48]. In particular, for typical ZSM-5 nanosheets, hydrocarbons have a high adsorption-desorption rate on the surface of the zeolite layers, and the internal diffusion effectiveness factor is close to 1 [49–52]. When used as a support to load metal active sites, the intercrystalline mesopores between individual layers can confine the metal NPs, and the ultrathin nanosheet layers facilitate the diffusion of reactants [53–55]. Although the metals supported on the ZSM-5 nanosheets have enhanced mass transfer and metal dispersion, the utilization of pristine micropores is impaired. The encapsulation of metal species in internal single-crystalline nanosheets can be interesting for realizing the high thermal stability of metal species, selectivity of microporous channels, and fast diffusion of reactants.

In this study, we developed sub-nanoscale Pt-Ni bimetals confined into hierarchically porous ZSM-5 zeolites composed of nanosheet aggregates (Pt-Ni@HZ) through a facile one-pot, seed-induced strategy. The introduction of nanocrystalline seeds accelerates the nucleation of the two-dimensional zeolite, promoting the coating of the metal precursor inside the zeolite. In hydrodeoxygenation (HDO) of lignin-derived phenolics, the uniformly distributed Pt-Ni alloys in the Pt-Ni@HZ catalyst significantly facilitated the sequential adsorption, activation, and transfer of active hydrogen, and the nanosheet layers with abundant intercrystalline pores facilitated the diffusion and adsorption of phenolics. In contrast to the conventional microporous ZSM-5 zeolite (CZ) and hierarchically porous ZSM-5 zeolite supporting Pt-Ni via impregnation (Pt-Ni/CZ and Pt-Ni/HZ, respectively), the prepared Pt-Ni@HZ exhibited almost 100 % conversion of anisole, with 95 % selectivity for cyclohexane under mild reaction conditions. In addition, the Pt-Ni@HZ catalyst exhibited excellent stability owing to the good structural stability of the metal species and low metal leaching.

2. Experiment

2.1. Materials

Detailed purchase information about the materials is in Supporting information.

2.2. Preparation of catalysts

Silicalite-1 nanocrystal seeds were synthesized using a previously reported hydrothermal method [56]. Typically, a mixture was prepared using tetraethoxysilane (TEOS) as the Si source and tetrapropylammonium hydroxide (TPAOH) as a template at a TPAOH: TEOS: H_2O molar ratio of 1: 2.8: 40. The obtained solution was aged by stirring at ambient temperature for 24 h. Then, the solution was autoclaved at 80 ℃ for 72 h. The final nanocrystalline seeds were obtained after calcination in air

at 550 ℃ for 6 h.

The ethylenediamine-complexed Pt-Ni solution was prepared by mixing 0.6061 g Pt solution (4.17 wt% H_2PtCl_6 in H_2O), 0.7133 g Ni $(NO_3)_2$ solution (10.48 wt% in H_2O), and 0.1820 g ethylenediamine. Pt-Ni bimetals encapsulated in HZ were prepared using a one-pot method. The mixture was first prepared with TEOS, aluminum isopropoxide (AIP), and tetrabutylphosphonium hydroxide (TBPOH) as the Si source, Al source, and template, respectively. The TEOS: AIP: TBPOH: NaOH: H_2O molar ratio was 10: 0.1: 1.5: 0.125: 100. AIP (0.0817 g), TBPOH (4.1466 g, 40 wt% in H_2O), NaOH solution (0.52 g, 1 M) and H_2O (4.212 g) were mixed. TEOS (7.92 g) was added to the solution and stirred for 6 h at ambient temperature. Silicalite-1 nanocrystal seeds (0.12 g, 5 wt% of the total Si source) and Pt-Ni solution were then added and stirred for 1 h. The resultant gel was placed in a Teflon-lined stainless steel autoclave at 130 ℃ for 48 h. Subsequently, the product was filtered, dried at 120 ℃ for 6 h and then calcined at 550 ℃ for another 6 h. To obtain the protonated zeolite samples, the synthesized catalyst (1 g) was added to an NH_4Cl (1 M, 150 mL) solution and stirred at 85 ℃ for 4 h. Subsequently, the product was washed, dried at 120 ℃ for 12 h, and calcined at 550 ℃ for 6 h. The final product with hierarchical pores was labeled Pt-Ni@HZ.

Pt-Ni bimetals loaded onto HZ by the wetness impregnation method were labeled Pt-Ni/HZ. The protonated HZ was synthesized under the same conditions, but without the addition of metal precursors. The metal solution was prepared by mixing 0.0664 g of H_2PtCl_6·6 H_2O, 0.2480 g of $Ni(NO_3)_2$·6 H_2O, and 9 g of H_2O. The theoretical loadings of Pt and Ni in the Pt-Ni/HZ catalyst were 0.5 and 1 wt%, respectively. The microporous ZSM-5 zeolite was synthesized using TPAOH as a template, as described in our previous study [57]. For comparison, Pt-Ni bimetals were loaded onto conventional microporous ZSM-5 zeolites by impregnation method and were labeled as Pt-Ni/CZ.

2.3. Measurements of HDO activities

HDO of anisole and guaiacol was performed in a 100 mL stainless steel batch autoclave. For a single run, 0.1 g of the catalyst, 0.5 g of reactant, and 30 mL of *n*-dodecane were placed in the reactor. After five hydrogen replacements, the initial pressure of hydrogen (99.9 vol%) was maintained at 3 MPa. The temperature was increased to the target temperature (150 °C for anisole and 200 °C for guaiacol), and the product mixture was removed at regular intervals. The reaction mixture was analyzed on a gas chromatograph (GC-7980, Techcomp, Beijing, China) equipped with a flame ionization detector and an HP-5 column (30 m × 0.52 mm × 5 μm).

2.4. Material characterization

Detailed characterization methods are in Supporting information.

3. Results and discussion

3.1. Characterizations

Fig. 1 illustrates the synthetic design strategies of the different catalysts. CZ and HZ were hydrothermally synthesized using TPAOH and TBPOH, respectively, as the templates. Conventionally, Pt-Ni/CZ and Pt-Ni/HZ were synthesized by wetness impregnation (Figs. 1a and b, respectively), wherein the metal species were mainly distributed on the surface of the zeolite support. The Pt-Ni@HZ catalyst was prepared by a one-pot method (Fig. 1c). Ethylenediamine-complexed Pt and Ni metal precursors can protect the metal species from precipitation in alkaline solutions. The use of TBPOH as a template can generate two-dimensional crystalline zeolites. The addition of nanocrystalline silicalite-1 seeds (S-1) to the synthetic solution accelerated the nucleation of zeolite, which facilitated the deposition of Pt-Ni metal precursors inside the nanosheet layers. After sequential hydrothermal
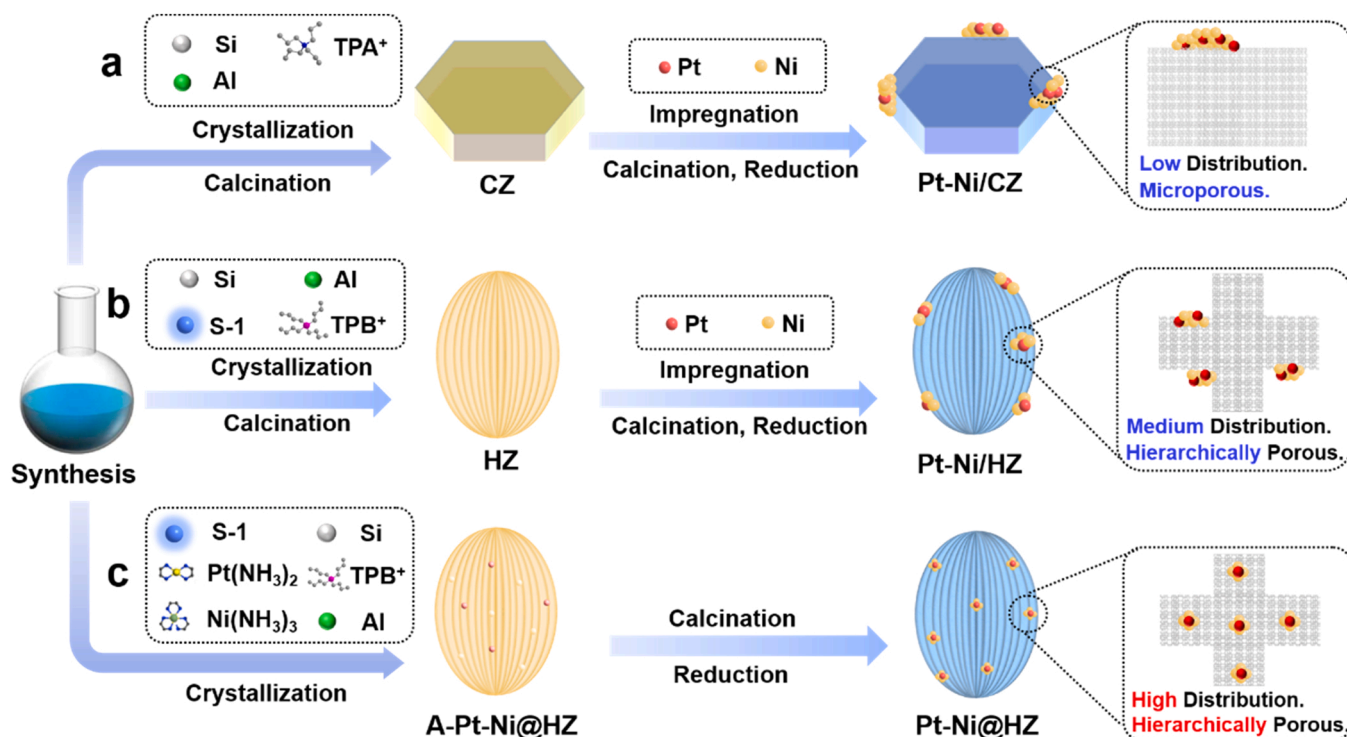
Fig. 1. Schematic illustration of the synthetic design of (a) Pt-Ni/CZ, (b) Pt-Ni/HZ, and (c) Pt-Ni@HZ.

synthesis, calcination, and reduction, the Pt-Ni bimetallic particles were encapsulated inside the zeolite nanosheet crystals. The obtained Pt-Ni@HZ catalyst had hierarchical pores owing to the aggregation of zeolite nanosheets and uniformly distributed metal active sites, which were expected to endow high catalytic activity and high thermal stability.

Pt-Ni@HZ (Fig. S1a) and Pt-Ni/HZ (Fig. S1b) exhibited a ship-type morphology, while Pt-Ni/CZ (Fig. S1c) exhibited a hexagonal morphology. The structures of the catalysts were further investigated by transmission electron microscopy (TEM). Pt-Ni/CZ (Fig. 2a) had a bulky crystalline structure, while Pt-Ni/HZ (Fig. 2b) and Pt-Ni@HZ (Fig. 2c) are composed of aggregated nanosheets with an individual thickness of ~10 nm (Fig. 2d and Fig. S2). The particle sizes of Ni on Pt-Ni/CZ (Fig. 2a') and Pt-Ni/HZ (Fig. 2b') were ~17.0 and ~2.9 nm, respectively. In contrast, highly dispersed metal species (Fig. 2e) with a sub-nanometric particle size of ~0.9 nm were observed inside Pt-Ni@HZ (Fig. 2c'). The *d*-spacing of the metal nanoparticles in Pt-Ni@HZ (Fig. 2f) and Pt-Ni/HZ (Fig. S3) was 0.213 nm and could be associated with the (111) NiPt plane (JCPDS 65–9446), indicating the formation of a Pt-Ni alloy [8]. HAADF-STEM energy-dispersive X-ray spectroscopy mapping also revealed the presence of highly distributed Pt and Ni species in the Pt-Ni@HZ catalyst (Fig. 2g). The Pt and Ni loadings (Table S1) were determined to be ~0.45 wt% and ~0.95 wt%, respectively, which are close to their theoretical loadings during synthesis. CO chemisorption studies (Table S1) revealed that the metal dispersion (D_M) decreased in the order Pt-Ni@HZ > Pt-Ni/HZ > Pt-Ni/CZ (details of the calculation are provided in the Supporting information file), which was in agreement with the TEM analysis. In contrast to the microporous zeolites, the nanosheet structures of Pt-Ni@HZ and Pt-Ni/HZ provided more exposed surfaces and facilitated the diffusion of reactants.

X-ray diffraction (XRD) measurements were performed to investigate the crystal phases of Pt-Ni@HZ, Pt-Ni/HZ, and Pt-Ni/CZ (Fig. 3a). All the samples exhibited a typical MFI crystalline phase (JCPDS 46–0003). [51] A weak peak ascribable to the Ni (111) crystalline phase was detected for Pt-Ni/CZ, indicating the aggregation of Ni on the zeolite surface. No notable diffraction peaks of the metal species were detected

for Pt-Ni/HZ and Pt-Ni@HZ; this can be attributed to the efficient dispersion of the metal species without the formation of bulk Ni. Fig. 3b shows the N₂-physisorption isotherms of the prepared samples. Pt-Ni/CZ exhibited a type-I isotherm, indicating a microporous structure, while Pt-Ni/HZ and Pt-Ni@HZ exhibited type-IV isotherm, indicating meso-porous structures [58,59]. The pore size distributions calculated using the non-local density functional theory for the adsorption branch are shown in Fig. 3c. The mesopores between the zeolite nanosheet nano-crystals in Pt-Ni/HZ and Pt-Ni@HZ were 2–5 nm in size. However, almost no mesopore distribution was detected for the Pt-Ni/CZ catalyst. This suggested that the numerous mesopores generated in Pt-Ni/HZ and Pt-Ni@HZ by the seed-induced method promoted the diffusion of re-actants. To investigate the interaction between the metal and zeolite, temperature-programmed reduction of H₂ (H₂-TPR) was performed (Fig. 3d). All catalysts were subjected to calcination in air at 550 °C for 6 h, without reduction. The peaks observed at temperatures lower than 350 °C are attributed to the reduction of Pt species. The reduction peaks of Ni are higher than 350 °C and can be decomposed into three sections, labeled as Peak I, II, and III, respectively. These peaks are ascribed to the reduction of different NiOₓ species with weak, medium, and strong interaction with the zeolite support [60]. The proportions of each peaks in H₂–TPR profiles are shown in Table S2. It is detected that the pro-portion of Ni–III in the prepared catalysts increased as Pt–Ni/CZ< Pt–Ni/HZ< Pt–Ni@HZ. Strong interaction between metal and zeolite could benefit the dispersion of metal species, which is consistent with TEM and CO–chemisorption detection. It is supposed that, hierarchical zeolite with enhanced exposed surfaces could provide more exposed sites which could anchor metal species, thereby increasing the metal dispersion through enhanced metal–carrier in-teractions. The metal-zeolite interactions in Pt-Ni/HZ and Pt-Ni@HZ significantly increased, which can be attributed to their exposed sur-faces [61].

The chemical environment of the metal species in the prepared cat-alysts was investigated by X-ray photoelectron spectroscopy (XPS; Fig. 3e), which is a surface-sensitive technique for detection up to a depth lower than 10 nm. The lowest intensity for both Ni 2*p* and Pt 4*d*
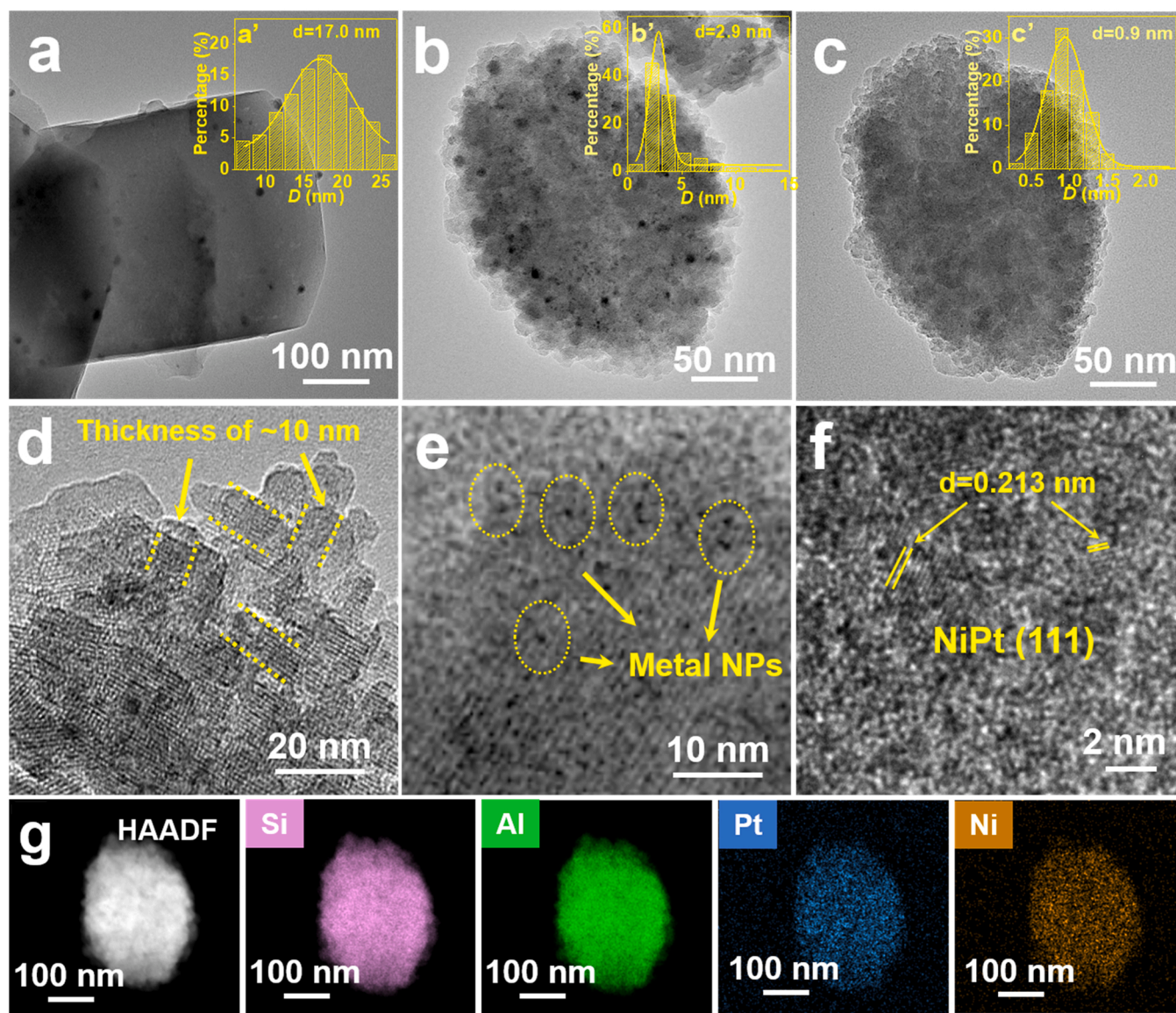
Fig. 2. TEM images of (a) Pt-Ni/CZ, (b) Pt-Ni/HZ, and (c) Pt-Ni@HZ (metal particle size distributions (a', b', c') are shown in the inset). TEM images of Pt-Ni@HZ at different magnifications (d, e, f), picture inserts in f: intensity profile obtained at selected locations (red rectangle); (g) HAADF-STEM Element mappings of Pt-Ni@HZ.

peaks is observed for Pt-Ni@HZ, implying that most Pt-Ni species are located in the interior of the zeolite [44]. In contrast, more metal species were deposited on the surface of the Pt-Ni/CZ. The spin-orbit coupling peaks of all the catalysts at binding energies of 851–868 eV were ascribed to Ni $2p_{3/2}$ [11]. The peaks at ~853 eV (red) and ~856 eV (blue) were attributed to Ni^0 and Ni^{2+}, respectively. In addition, a satellite peak was observed at ~862 eV [11]. Peak deconvolution (Table S3) suggested that the binding energies of Ni^{2+} in Pt-Ni/HZ and Pt-Ni@HZ shifted to higher values compared to that of Pt-Ni/CZ, implying stronger interactions between the zeolite and Ni in Pt-Ni/HZ and Pt-Ni@HZ. This conclusion was consistent with the H_2-TPR analysis. The strong metal-zeolite interaction improved the dispersion of metal species, in agreement with the TEM and CO chemisorption analyses.

X-ray absorption near edge structure (XANES, Fig. 3f) and extended X-ray absorption fine structure (EXAFS, Fig. 3g) spectra provided detailed structural information on the metal species in the zeolites. The XANES spectral intensities of Pt-Ni/CZ and Pt-Ni@HZ were slightly higher than that of Pt foil and shifted to higher energy values, implying Pt-X (O and/or Ni) bonding, except Pt-Pt bonding. EXAFS spectra

revealed the dominant Pt-O and Pt-Ni bonds in the prepared samples. Coordination numbers (CN) of Pt-O bonding in Pt-Ni@HZ (1.8) and Pt-Ni/CZ (1.4), are much lower than that of isaolated PtO_2 (6.1) as shown in Fig. S4. It is inferred that the Pt-O bonds in Pt-Ni/CZ and Pt-Ni@HZ originated from the zeolite framework. The CN of Pt-O was higher for Pt-Ni@HZ, implying strong metal-oxygen interactions that could promote metal dispersion with interaction with the zeolite framework. Moreover, the CN of the Pt-Pt bonds in Pt-Ni@HZ was lower than that in Pt-Ni/CZ, whereas the CN of the Pt-Ni bonds showed the opposite trend. This indicated that Pt was highly dispersed in the Pt-Ni alloy of Pt-Ni@HZ, consistent with the HR-TEM images. Similar result was also drawn from the Ni K-edge XAS spectra of bi-metallic Pt-Ni samples. Most of the spectral features of Pt-Ni alloy NPs, are similar to those of previously reported Pt-Ni alloy NPs and different from the Ni foil sample [62]. From the XANES spectras (Fig. S4a), the Pt-Ni are enclosing a weak pre-edge feature ~8322 eV, which is similar to the Ni foil, indicating the exist of Ni-Ni bonds. Besides intensities of Pt-Ni/CZ and Pt-Ni@HZ were higher than that of Ni foil, implying Ni-O bonding, except Ni-Ni bonding. EXAFS spectra revealed the dominant Ni-O and Pt-M (Ni or Pt) bonds in the prepared samples (Fig. S4b). The coordination number (CN) of Ni-O
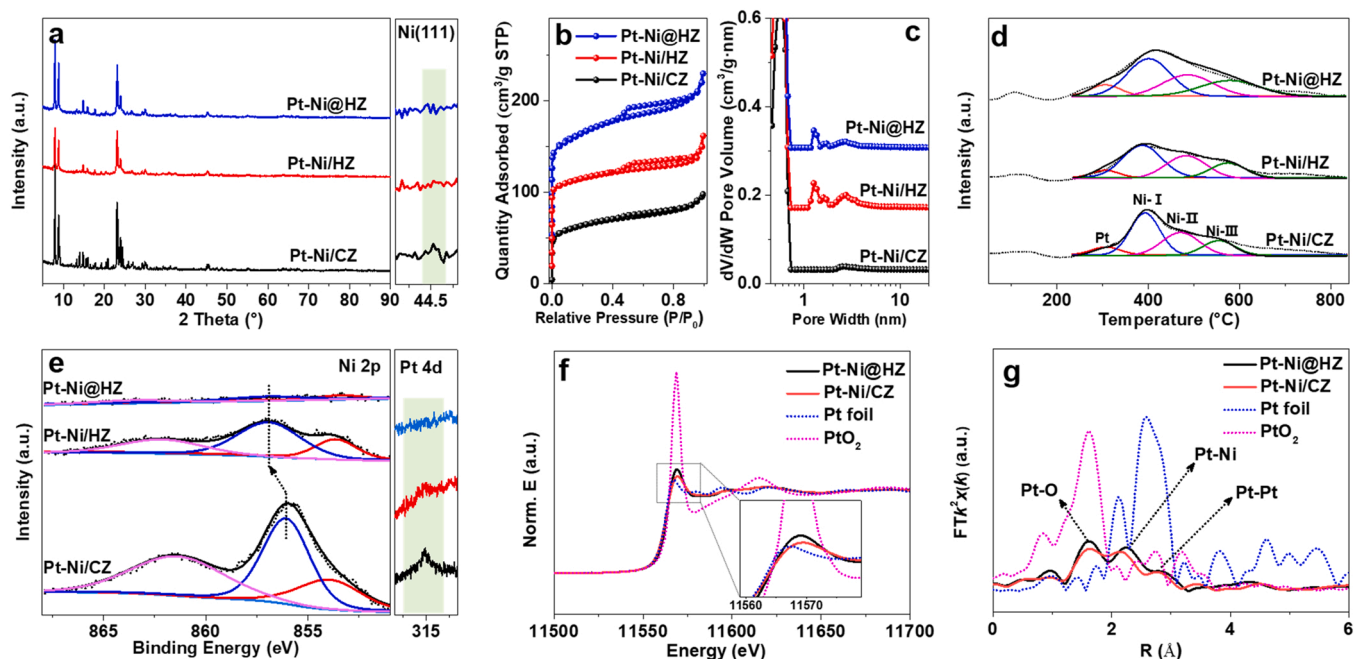
Fig. 3. Characterization of Pt-Ni@HZ, Pt-Ni/HZ, and Pt-Ni/CZ: (a) XRD patterns, (b) N$_2$-physisorption isotherms, (c) pore size distributions, (d) H$_2$-TPR profiles, (e) XPS spectra. (f) Pt L3-edge XANES spectra, and (g) Pt L3-edge EXAFS spectra of the prepared catalysts.

was higher in Pt-Ni@HZ than that in Pt-Ni/CZ, implying strong metal-oxygen interactions in Pt-Ni@HZ (Table S5). While the CN of Ni-M of Pt-Ni@HZ is relative lower than that in Pt-Ni/CZ, implying the smaller metal species in the samples prepared by one-pot synthesis method.

3.2. HDO Performance

The HDO of anisole was selected as a model reaction to explore the catalytic performance of the prepared catalysts. Fig. 4a shows the time-dependent conversions of anisole using Pt-Ni/CZ, Pt-Ni/HZ, and Pt-Ni@HZ as catalysts at 150 °C. At any particular reaction time, the anisole conversion decreased in the order Pt-Ni@HZ > Pt-Ni/HZ > Pt-Ni/CZ. After 180 min of reaction, anisole conversion in the presence of Pt-Ni@HZ and Pt-Ni/HZ reached almost 100 %, which was significantly higher than that in the presence of Pt-Ni/CZ catalyst (47.6 %) after the same reaction time. The turnover frequencies (TOFs) of reactant conversion based on the surface metal species revealed different catalytic activities (Fig. 4b). At a reaction time of 5 min and conversion below 20 % (kinetic region), the TOF for Pt-Ni@HZ was relatively higher than those of Pt-Ni/HZ and Pt-Ni/CZ.

Four products, namely, cyclohexane, cyclohexene, cyclohexanol (or cyclohexanone), and methoxycyclohexane, were detected in the product (Fig. 4c). Detailed product distribution with time is shown in Fig. S5. By the Pt-Ni/CZ catalyst (Fig. S5a), the selectivity of methoxycyclohexane, cyclohexanol decrease, while which of cyclohexene and cyclohexane increase. For the Pt-Ni/HZ (Fig. S5b) and Pt-Ni@HZ (Fig. S5c) catalysts, only selectivity of cyclohexane increase and other product decrease with time. Pt-Ni@HZ sample affords the highest achievement of cyclohexane. As shown in Fig. S5d, it is assumed that anisole undergoes hydrogenation via the formation of methoxycyclohexane under high H$_2$ pressure [63]. Metal active sites accept the delocalized aromatic ring electron, resulting in the activation of the ring, which allowed the nucleophilic addition reaction to happen through the adsorbed H attacking the aromatic rings [64]. Then methoxycyclohexane goes through sequenced demethylation with formation of cyclohexanol, dehydration with the formation of cyclohexene and hydrogenation with the formation of the final product cyclohexane. The selectivity of Pt-Ni@HZ toward

cyclohexane was relatively high (~94.5 wt%), while the selectivities of Pt-Ni/HZ and Pt-Ni/CZ were relatively low (~81.4 % and ~56.6 %, respectively). Thus, the uniformly distributed metal species and improved diffusion pathways in the Pt-Ni@HZ catalyst facilitate the deep hydrogenation and deoxygenation of phenolics. It was encouraging to find that the excellent catalytic HDO performance of Pt-Ni@HZ was better than that of the previously reported catalysts (Table S6). Here, The diffusivities of anisole in the prepared catalyst is detected by the Zero–Length Column Method (ZLC) [65]. The desorption curves of anisole and the fitting results was shown in Fig. S6 and Table S7, respectively. In general, the Pt-Ni/HZ and Pt-Ni@HZ catalysts afford almost 3 times higher diffusion efficiency (D_{effe}) values compared with Pt-Ni/CZ catalyst, at both two temperatures (40 °C and 100 °C), evidencing the promoted diffusivity by hierarchical pore structure.

In the presence of zeolite-supported metal catalysts, the HDO is highly dependent on acid properties and metal species [7,66]. The acid sites associated with zeolites influence the adsorption of phenolic compounds, while metal sites adsorb and activate hydrogen. The activated hydrogen species are transferred through the metal-zeolite interface to react with the phenolic compounds adsorbed on the catalyst surface. To explore the acidic properties of Pt-Ni/CZ, Pt-Ni/HZ, and Pt-Ni@HZ, temperature-programmed desorption of ammonium (NH$_3$-TPD) was performed. As shown in Fig. 4d, the peaks at ~250 and ~450 °C were ascribed to the weak and strong acid sites, respectively. The total acidity was similar for all the catalysts, which was consistent with the Al concentration in the catalysts (Table S8). Moreover, pyridine-adsorbed infrared spectroscopy (Py-IR) revealed the Lewis and Brønsted acid sites on the prepared catalysts (Fig. S7). The peaks at ~1452 and ~1543 cm^{-1} correspond to the interaction of pyridine with Lewis and Brønsted acid sites, respectively [67]. The Pt-Ni@HZ catalyst exhibited increased Lewis acidity and decreased Brønsted acidity compared to the other two catalysts. It is inferred that high dispersed metal species with strong Metal-O interaction formed between Ni and the surface hydroxyl groups in Pt-Ni@HZ at the expense of Brønsted acid bonds (Si-O-Al) [68]. The anisole-adsorbed IR spectrum (Fig. 4e) was obtained to determine the amount of anisole adsorbed on the prepared catalysts. The peaks at ~1600/1500 and ~1450 cm^{-1} were related to the hydroxyl and methyl groups in anisole, respectively. The peak
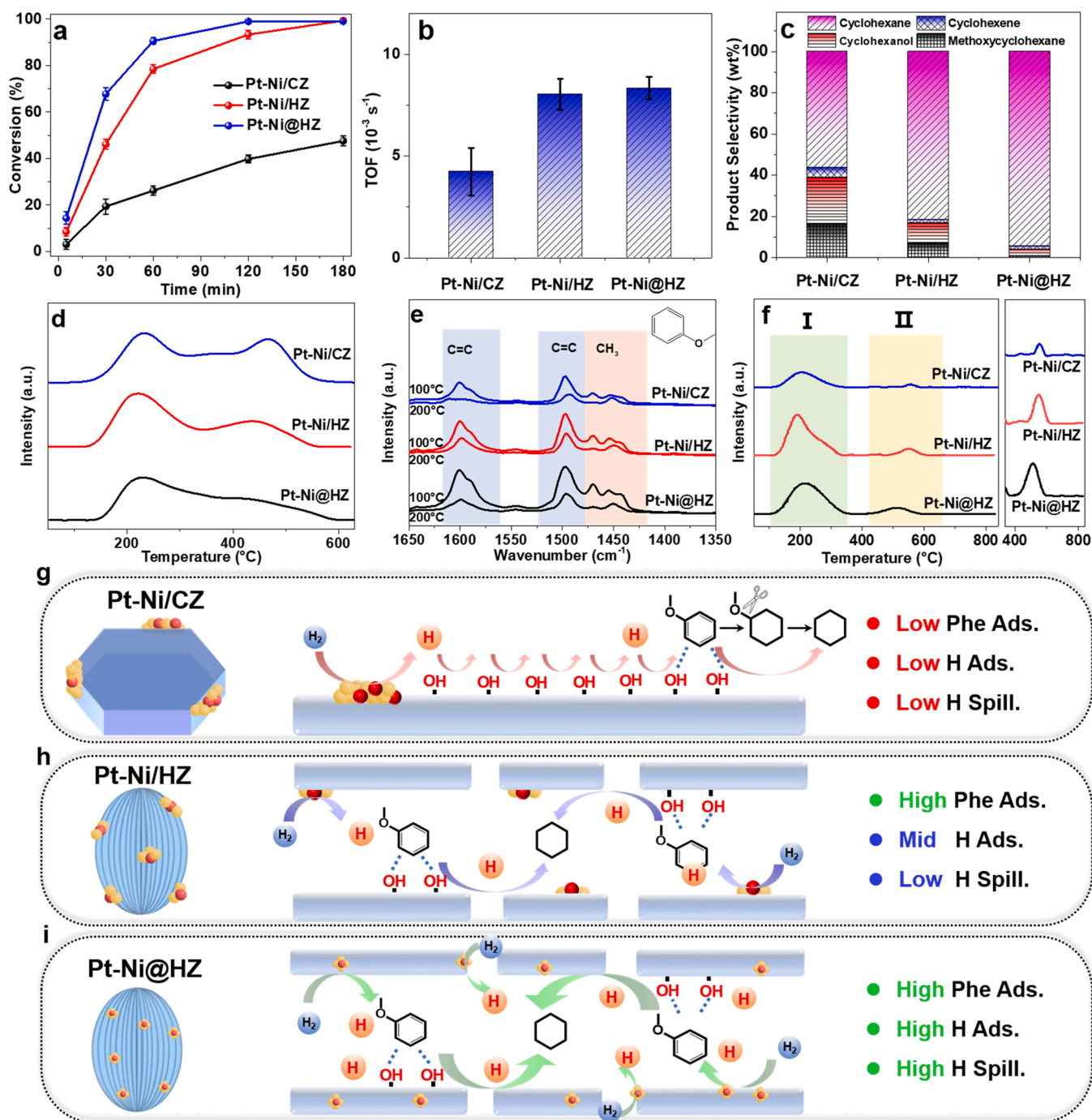
Fig. 4. HDO anisole: (a) conversion profile with time, (b) TOFs at 5 min, and (c) detailed product distribution at 180 min (d) NH$_3$-TPD profiles, (e) anisole-adsorbed IR spectra, and (f) H$_2$-TPD profiles of the catalyst. Schematic illustration of the different diffusion pathways and metal dispersion for (g) Pt-Ni/CZ, (h) Pt-Ni/HZ, and (i) Pt-Ni@HZ.

intensities suggest that the adsorption of anisole by Pt-Ni@HZ and Pt-Ni/HZ was significantly higher than that by Pt-Ni/CZ. Considering the similar acidities of Pt-Ni@HZ and Pt-Ni/HZ, it is speculated that these Pt-Ni@LZ catalyst with highly dispersed metal species could promote the adsorption of anisole.

FTIR of the prepared ZSM–5 zeolite was further performed to reveal the acid properties (Fig. S8a). All the zeolites were pretreated in a sealed chamber under vacuum (P < 0.1 Par) at 500 °C for 2 h, to eliminate the influence of adsorbed H$_2$O. Band with wavenumber of ~3610 cm^{-1} is ascribed to the bridging hydroxyl groups association with Brønsted acid sites, which intensity decreases as Pt–Ni/CZ>Pt–Ni/HZ≈Pt–Ni@HZ,

partially consistent with Py–IR result. Moreover, the peak with wavenumber of ~3670 cm^{-1} are ascribed to Al(OH)$_x$, which composes of extra–framework Al species (EF–AL) in ZSM–5 zeolite [69]. Generally, EF–Al is association with Lewis acid sites. Almost no EF–AL for all the three catalysts, suggesting that the Lewis acid sites in the prepared catalyst is correlated with the introduced metal species. Fig. S8b shows the ^{27}Al MAS NMR spectra of the catalysts, peaks at ~55 and ~1 ppm is attributed to the tetrahedrally coordinated framework Al (F–Al association with Brønsted acid sites) and the octahedral coordinated EF–Al, respectively [70]. For all the three catalysts, almost no extra–framework Al is detected, consistent with IR result.

To investigate the adsorption and transfer of hydrogen, temperature-programmed desorption of hydrogen (H₂-TPD) was performed. As shown in Fig. 4f, peaks below and above 400 °C are ascribed to the adsorbed hydrogen (I) and spillover hydrogen (II), respectively. H₂ molecules are first adsorbed on the surface of the metal to form active protons, which are transferred through the metal-zeolite interface to react with the phenolic compounds on the acid sites of the zeolite. The H₂ adsorption capacities of the Pt-Ni/HZ and Pt-Ni@HZ catalysts were significantly higher than that of the Pt-Ni/CZ catalyst (Table S8). Moreover, the Pt-Ni@HZ catalyst exhibited the highest amount of spillover H₂ among the prepared catalysts. This demonstrates that the highly dispersed Pt-Ni species not only promote hydrogen adsorption but also provide more metal-zeolite interfaces that can facilitate the transfer of active protons [71].

Based on the above discussion, the structures and reaction routes of the prepared catalysts were analyzed. For the Pt-Ni/CZ catalyst with only micropores (Fig. 4g), the diffusion of the reactant was restricted, which decreased the adsorption of anisole. Moreover, the metal species aggregate on the zeolite surface, deteriorating the adsorption and transfer of active hydrogen and reducing the catalytic activity. For the Pt-Ni/HZ catalyst, the good distribution of the metal active sites benefited the adsorption of hydrogen. Furthermore, the adsorption of anisole and spillover of active hydrogen were promoted by the hierarchical pore structure with exposed surface areas (Fig. 4h), thus resulting

in relatively high TOFs in the HDO of phenolics. For the Pt-Ni@HZ catalyst (Fig. 4i) with hierarchical pores and highly dispersed metal species inside the zeolite crystal, the synergistic effect of acid and metal sites led to enhanced catalytic activity. Therefore, the hierarchical pores and uniformly dispersed metal active sites significantly improved the diffusion kinetics and facilitated the adsorption/transfer of hydrogen, resulting in excellent catalytic HDO performance of anisole with high selectivity toward cyclohexane.

To further explore the catalytic HDO performance of the prepared catalysts, guaiacol, with hydroxyl and methoxy substituents on benzene, was selected as another reactant. The conversion over time at 200 °C is shown in Fig. 5a. The Pt-Ni@HZ catalyst exhibits the best catalytic performance, with the highest TOF at the beginning (5 min) of the reaction (Fig. 5b). The detailed product yields are shown in Fig. 5c and product distribution with time is shown in Fig. S9. Cyclohenaxne is the final product with increased selectivity in the product by all the prepared catalyst. 2,6-methoxycyclohexanol and phenol are detected in the product, while trace amount of anisole is detected. This result demonstrates that hydrogenation (with the formation of 2,6-methoxycyclohexanol) and/or demethoxygenation (with the formation of phenol) happens. The reported oxophilic sites by transition metal catalysts (Ni) could favor the direct deoxygenation of guaiacol, which support the conclusion [72]. Moreover, the direct hydrogenation of aromatic ring on the active site is also easily realized with benzene ring adsorbed on the acid sites of zeolite [73]. After
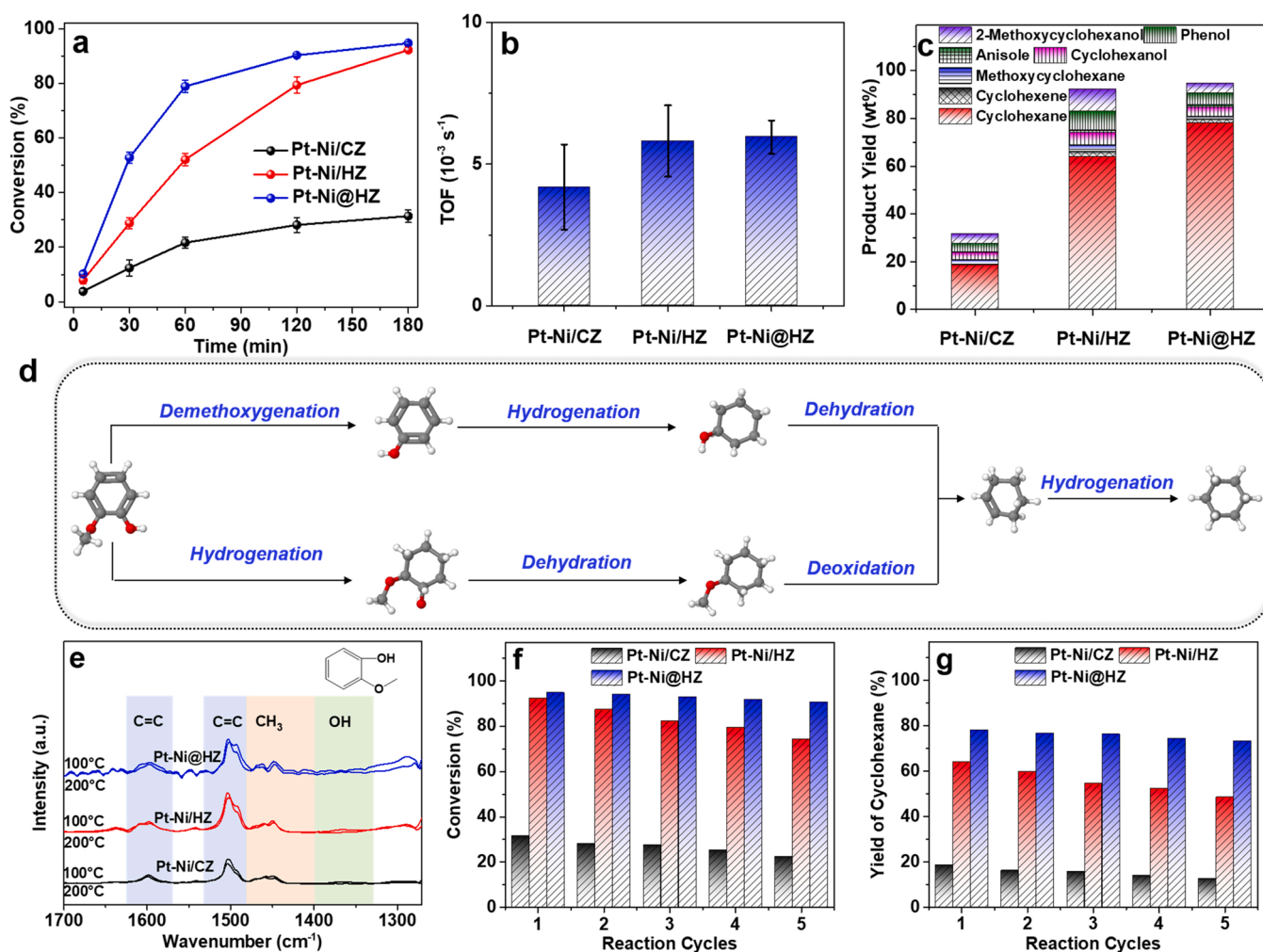

Fig. 5. HDO performance of guaiacol: (a) conversion profile with time, (b) TOFs at a reaction time of 5 min, (c) detailed product yield at 180 min, (d) proposed reaction pathway, and (e) guaiacol-adsorbed IR spectrum of the prepared catalysts. (f) Catalytic stability for five cycles and (g) yield of cyclohexane using the prepared catalysts.

that, produced phenol and 2,6-methoxycyclohexanol goes through sequenced (hydrogenation-dehydration-hydrogenation) and (dehydration-demethoxygenation-hydrogenation) pathways respectively, with the final product of cyclohexane (Fig. 5d). The yield of cyclohexane using the Pt-Ni@HZ catalyst reached up to 78.5 wt%, which was higher than that obtained using the Pt-Ni/HZ and Pt-Ni/CZ catalysts. The FT-IR spectra of guaiacol adsorption (Fig. 5e) further revealed the enhanced adsorption of guaiacol on the Pt-Ni@HZ catalyst, and this benefited the catalytic HDO performance.

To explore the stability of the prepared catalysts, the spent catalysts were separated, dried (100 °C for 4 h), calcined (550 °C for 4 h), and reduced (600 °C for 2 h). These recycled catalysts were used for a fresh HDO reaction of anisole. The conversion decreased with increased recycling of the catalysts (Fig. 5f). The Pt-Ni@HZ catalyst exhibited better stability (Table S9), with a low deactivation rate (r_d) of 4.4 % compared with that of Pt-Ni/HZ (11.9 %) and Pt-Ni/CZ (19.1 %). After five cycles (Fig. 5g), the yield of cyclohexane was relatively high using the Pt-Ni@HZ catalyst. The spent catalysts (S-catalysts) were analyzed by inductively coupled plasma-optical emission spectrometry (ICP-OES) to determine metal leaching during the reaction. ICP-OES revealed that the leaching of Pt and/or Ni from S-Pt-Ni@HZ was lower than that from the other catalysts, implying the good stability of the metal species inside the zeolite (Table S9). TEM images provided further information on the distribution of the metal species in the spent catalysts (Fig. S10). The metal species remained stable in the Pt-Ni@HZ catalyst without obvious aggregation even after five cycles of reaction (Fig. S10a), whereas they gathered on the surface of the Pt-Ni/HZ (Fig. S10b) and Pt-Ni/CZ (Fig. S10c) catalysts. The excellent catalytic stability of Pt-Ni@HZ was attributed to the protective zeolite framework.

4. Conclusion

In summary, we discovered an efficient strategy for promoting the HDO of phenolics over hierarchical Pt-Ni@HZ nanosheets. The Pt-Ni metal species were distributed uniformly in the zeolite nanosheet layers by the virtue of strong metal-zeolite interactions. The intercrystalline mesopores constructed by the nanosheet layers promoted the adsorption of reactants, and the highly dispersed metal species facilitated the adsorption and transfer of active hydrogen. Moreover, the metal species encapsulated in the zeolite channels promoted deoxygenation via synergistic interactions with the zeolite framework, affording high yields of cyclohexane. With relatively low Pt and Ni loadings (0.5 and 1 wt%, respectively), the anisole conversion reached almost 100 % over the Pt-Ni@HZ catalyst, with 94.5 % selectivity toward cyclohexane at 150 °C. After five reaction cycles, the least metal leaching (1.3 wt%) and best stability of the metal species were observed for the Pt-Ni@HZ catalyst. This work provides a prototype for boosting the reactivity and selectivity through the rational tuning of the catalytic hydrodeoxygenation reaction.

CRediT authorship contribution statement

Yajie Tian: Conceptualization, Formal analysis, Data curation, Writing-review & editing.**Longhui Guo**:Investigation, Writing-original draft. **Congzhen Qiao**:Writing-review & editing. **Zixu Sun**:Investigation, Data curation. **Yusuke Yamauchi**: Writing-review & editing. **Shude Liu**: Investigation, Formal analysis, Writing-review & editing.

Declaration of Competing Interest

The authors declare that they have no known competing financial interests or personal relationships that could have appeared to influence the work reported in this paper.

Data availability

Data will be made available on request.

Supporting Information

The Supporting Information is available free of charge on the website. Materials, methods, supporting Figures, and tables (PDF).

Appendix A. Supporting information

Supplementary data associated with this article can be found in the online version at doi:10.1016/j.apcatb.2023.122945.

References

[1] W. Liu, Y. Yang, L. Chen, E. Xu, J. Xu, S. Hong, X. Zhang, M. Wei, Atomically-ordered active sites in NiMo intermetallic compound toward low-pressure hydrodeoxygenation of furfural, Appl. Catal. B: Environ. 282 (2021), 119569.

[2] G. Moos, M. Emondts, A. Bordet, W. Leitner, Selective hydrogenation and hydrodeoxygenation of aromatic ketones to cyclohexane derivatives using a Rh@SILP catalyst, Angew. Chem. Int. Ed. 59 (2020) 2–9.

[3] F. Yang, D. Liu, Y. Zhao, H. Wang, J. Han, Q. Ge, X. Zhu, Size dependence of vapor phase hydrodeoxygenation of m-Cresol on Ni/SiO$_2$ catalysts, ACS Catal. 8 (2018) 1672–1682.

[4] X. Zhang, W. Tang, Q. Zhang, T. Wang, L. Ma, Hydrodeoxygenation of lignin-derived phenoic compounds to hydrocarbon fuel over supported Ni-based catalysts, Appl. Energy 227 (2018) 73–79.

[5] X. Zhang, K. Wang, J. Chen, L. Zhu, S. Wang, Mild hydrogenation of bio-oil and its derived phenolic monomers over Pt–Ni bimetal-based catalysts, Appl. Energy 275 (2020), 115154.

[6] P. Yan, J. Mensah, M. Drewery, E. Kennedy, T. Maschmeyer, M. Stockenhuber, Role of metal support during ru-catalysed hydrodeoxygenation of biocrude oil, Appl. Catal. B: Environ. 281 (2021), 119470.

[7] P. Yan, E. Kennedy, M. Stockenhuber, Natural zeolite supported Ni catalysts for hydrodeoxygenation of anisole, Green Chem. 23 (2021) 4673–4684.

[8] S. Li, L. Guo, X. He, C. Qiao, Y. Tian, Synthesis of uniform Ni nanoparticles encapsulated in ZSM–5 for selective hydrodeoxygenation of phenolics, Renew. Energy 194 (2022) 89–99.

[9] H. Wang, Sa Wang, L. Guo, C. Qiao, Y. Tian, Hierarchical ZSM–5 supported Ni catalysts for hydrodeoxygenation of phenolics: effect of reactant volumes and substituents, Chem. Eng. J. (2023), 140647.

[10] W. Wang, L. Guo, X. He, L. Deng, C. Qiao, Y. Tian, Uniform Ni species encapsulated in nanocrystalline ZSM–5 with enhanced catalytic performance for upgrading of fatty acids, Fuel 346 (2023), 128411.

[11] G. Chen, J. Liu, X. Li, J. Zhang, H. Yin, Z. Su, Investigation on catalytic hydrodeoxygenation of eugenol blend with light fraction in bio-oil over Ni-based catalysts, Renew. Energy 157 (2020) 456–465.

[12] Y. Tian, H. Duan, B. Zhang, S. Gong, Z. Lu, L. Dai, C. Qiao, G. Liu, Y. Zhao, Template guiding for regioselective fabrication of uniformly sub-nanometric Pt clusters in beta-zeolites with high catalytic activity and stability, Angew. Chem. Int. Ed. 60 (2021) 21713–21717.

[13] L. Li, A. Cheruvathur, S. Zuo, P. An, F. Hou, J. Xu, G. Li, G. Liu, Surface structure modulating of Ni-Pt bimetallic catalysts boosts n-dodecane steam reforming, Appl. Catal. B: Environ. 299 (2021), 120670.

[14] W.W. Lonergan, D.G. Vlachos, J.G. Chen, Correlating extent of Pt–Ni bond formation with low-temperature hydrogenation of benzene and 1,3-butadiene over supported Pt/Ni bimetallic catalysts, J. Catal. 271 (2010) 239–250.

[15] Q. Sun, N. Wang, Q. Fan, L. Zeng, A. Mayoral, S. Miao, R. Yang, Z. Jiang, W. Zhou, J. Zhang, T. Zhang, J. Xu, P. Zhang, J. Cheng, D.C. Yang, R. Jia, L. Li, Q. Zhang, Y. Wang, O. Terasaki, J. Yu, Subnanometer bimetallic platinum–zinc clusters in

zeolites for propane dehydrogenation, Angew. Chem. Int. Ed. 59 (2020) 19450–19459.

[16] Q. Sun, N. Wang, Q. Bing, R. Si, J. Liu, R. Bai, P. Zhang, M. Jia, J. Yu, Subnanometric hybrid Pd-M(OH)₂, M= Ni, Co, clusters in zeolites as highly efficient nanocatalysts for hydrogen generation, Chem 3 (2017) 477–493.

[17] J. Wang, J. Shan, Y. Tian, T. Zhu, H. Duan, X. He, C. Qiao, G. Liu, Catalytic cracking of n-heptane over Fe modified HZSM-5 nanosheet to produce light olefins, Fuel 306 (2021), 121725.

[18] X. Yu, C. Zhou, Z. Huang, C. Xin, Y. Lin, F. Fu, S. Li, W. Zhang, Rational design of AgCl@Zr³⁺-ZrO₂ nanostructures for ultra-efficient visible-light photodegradation of emerging pollutants, Appl. Catal. B: Environ. 325 (2023), 122308.

[19] S. Wu, X. Yang, C. Janiak, Confinement effects in zeolite-confined noble metals, Angew. Chem. Int. Ed. 58 (2019) 12340–12354.

[20] J. Zhang, L. Wang, Y. Shao, Y. Wang, B.C. Gates, F.-S. Xiao, A Pd@Zeolite, Catalyst for nitroarene hydrogenation with high product selectivity by sterically controlled adsorption in the zeolite micropores, Angew. Chem. Int. Ed. 56 (2017) 9747–9751.

[21] Y. Chai, S. Liu, Z.-J. Zhao, J. Gong, W. Dai, G. Wu, N. Guan, L. Li, Selectivity modulation of encapsulated palladium nanoparticles by zeolite microenvironment for biomass catalytic upgrading, ACS Catal. 8 (2018) 8578–8589.

[22] L. Liu, M. Lopez-Haro, C.W. Lopes, S. Rojas-Buzo, P. Concepcion, R. Manzorro, L. Simonelli, A. Sattler, P. Serna, J.J. Calvino, A. Corma, Structural modulation and direct measurement of subnanometric bimetallic PtSn clusters confined in zeolites, Nat. Cat. 3 (2020) 628–638.

[23] T. Otto, S.I. Zones, Y. Hong, E. Iglesia, Synthesis of highly dispersed cobalt oxide clusters encapsulated within LTA zeolites, J. Catal. 356 (2017) 173–185.

[24] J. Zhu, R. Osuga, R. Ishikawa, N. Shibata, Y. Ikuhara, J.N. Kondo, M. Ogura, J. Yu, T. Wakihara, Z. Liu, T. Okubo, Ultrafast encapsulation of metal nanoclusters into MFI zeolite in the course of its crystallization: catalytic application for propane dehydrogenation, Angew. Chem. Int. Ed. 59 (2020) 1–7.

[25] H.J. Cho, D. Kim, J. Li, D. Su, B. Xu, Zeolite-encapsulated Pt nanoparticles for tandem catalysis, J. Am. Chem. Soc. 140 (2018) 13514–13520.

[26] X. Deng, B. Qin, R. Liu, X. Qin, W. Dai, G. Wu, N. Guan, D. Ma, L. Li, Zeolite-encaged isolated platinum ions enable heterolytic dihydrogen activation and selective hydrogenations, J. Am. Chem. Soc. 143 (2021) 20898–20906.

[27] L. Liu, M. Lopez-Haro, C.W. Lopes, C. Li, P. Concepcion, L. Simonelli, J.J. Calvino, A. Corma, Regioselective generation and reactivity control of subnanometric platinum clusters in zeolites for high-temperature catalysis, Nat. Mater. 18 (2019) 866–873.

[28] T. Iida, D. Zanchet, K. Ohara, T. Wakihara, Y. Román-Leshkov, Concerted bimetallic nanocluster synthesis and encapsulation via induced zeolite framework demetallation for shape and substrate selective heterogeneous catalysis, Angew. Chem. Int. Ed. 57 (2018) 6454–6458.

[29] M. Moliner, J. Gabay, C. Kliewer, P. Serna, A. Corma, Trapping of metal atoms and metal clusters by chabazite under severe redox stress, ACS Catal. 8 (2018) 9520–9528.

[30] L. Liu, A. Corma, Confining isolated atoms and clusters in crystalline porous materials for catalysis, Nat. Rev. Mater. 6 (2021) 244–263.

[31] S. Goel, S.I. Zones, E. Iglesia, Encapsulation of metal clusters within MFI via interzeolite transformations and direct hydrothermal syntheses and catalytic consequences of their confinement, J. Am. Chem. Soc. 136 (2014) 15280–15290.

[32] C. Gao, F. Lyu, Y. Yin, Encapsulated metal nanoparticles for catalysis, Chem. Rev. (2020) 834–881.

[33] S. Goel, Z. Wu, S.I. Zones, E. Iglesia, Synthesis and catalytic properties of metal clusters encapsulated within small-pore (SOD, GIS, ANA) zeolites, J. Am. Chem. Soc. 134 (2012) 17688–17695.

[34] D. Xu, H. Lv, B. Liu, Encapsulation of metal nanoparticle catalysts within mesoporous zeolites and their enhanced catalytic performances: a review, Front. Chem. 6 (2018) 550.

[35] D. Kerstens, B. Smeyers, J. Van Waeyenberg, Q. Zhang, J. Yu, B.F. Sels, State of the art and perspectives of hierarchical zeolites: practical overview of synthesis methods and use in catalysis, Adv. Mater. 32 (2020) e2004690.

[36] H. Konno, T. Okamura, T. Kawahara, Y. Nakasaka, T. Tago, T. Masuda, Kinetics of n-hexane cracking over ZSM-5 zeolites – effect of crystal size on effectiveness factor and catalyst lifetime, Chem. Eng. J. 207–208 (2012) 490–496.

[37] C. Li, P. Sun, F. Li, Hierarchical zeolites-confined metal catalysts and their enhanced catalytic performances, Chem. Asian J. 16 (2021) 2795–2805.

[38] I.C. Medeiros-Costa, E. Dib, N. Nesterenko, J.P. Dath, J.P. Gilson, S. Mintova, Silanol defect engineering and healing in zeolites: opportunities to fine-tune their properties and performances, Chem. Soc. Rev. 50 (2021) 11156–11179.

[39] J. Han, J. Cho, J.-C. Kim, R. Ryoo, Confinement of supported metal catalysts at high loading in the mesopore network of hierarchical zeolites, with access via the microporous windows, ACS Catal. 8 (2018) 876–879.

[40] X. Jia, J. Jiang, S. Zou, L. Han, H. Zhu, Q. Zhang, Y. Ma, P. Luo, P. Wu, A. Mayoral, X. Han, J. Cheng, S. Che, Library creation of ultrasmall multi-metallic nanoparticles confined in mesoporous MFI zeolites, Angew. Chem. Int. Ed. 60 (2021) 14571–14577.

[41] Q. Zhang, A. Mayoral, O. Terasaki, Q. Zhang, B. Ma, C. Zhao, G. Yang, J. Yu, Amino acid-assisted construction of single-crystalline hierarchical nanozeolites via oriented-aggregation and intraparticle ripening, J. Am. Chem. Soc. 141 (2019) 3772–3776.

[42] T. Cui, W. Ke, W. Zhang, H. Wang, X. Li, J. Chen, Encapsulating palladium nanoparticles inside mesoporous MFI zeolite nanocrystals for shape-selective catalysis, Angew. Chem. Int. Ed. 55 (2016) 9178–9182.

[43] J. Mielby, J.O. Abildstrom, F. Wang, T. Kasama, C. Weidenthaler, S. Kegnæs, Oxidation of bioethanol using zeolite-encapsulated gold nanoparticles, Angew. Chem. Int. Ed. 53 (2014) 12513–12516.

[44] N. Wang, Q. Sun, R. Bai, X. Li, G. Guo, J. Yu, In situ confinement of ultrasmall Pd clusters within nanosized silicalite-1 zeolite for highly efficient catalysis of hydrogen generation, J. Am. Chem. Soc. 138 (2016) 7484–7487.

[45] X. Shen, W. Mao, Y. Ma, D. Xu, P. Wu, O. Terasaki, L. Han, S. Che, A hierarchical MFI Zeolite with a Two-Dimensional Square Mesostructure, Angew. Chem. Int. Ed. 130 (2018) 732–736.

[46] G. Liu, Y. Tian, B. Zhang, L. Wang, X. Zhang, Catalytic combustion of VOC on sandwich-structured Pt@ZSM-5 nanosheets prepared by controllable intercalation, J. Hazard. Mater. 367 (2019) 568–576.

[47] N. Wang, Q. Sun, T. Zhang, A. Mayoral, L. Li, X. Zhou, J. Xu, P. Zhang, J. Yu, Impregnating subnanometer metallic nanocatalysts into self-pillared zeolite nanosheets, J. Am. Chem. Soc. 143 (2021) 6905–6914.

[48] Q. Guo, J. Zhao, Y. Yang, J. Huang, Y. Tang, X. Zhang, Z. Li, X. Yu, J. Shen, J. Zhao, Mesocrystalline Ta₃N₅ superstructures with long-lived charges for improved visible light photocatalytic hydrogen production, J. Colloid Interface Sci. 560 (2020) 359–368.

[49] M. Choi, K. Na, J. Kim, Y. Sakamoto, O. Terasaki, R. Ryoo, Stable single-unit-cell nanosheets of zeolite MFI as active and long-lived catalysts, Nature 461 (2009) 246–249.

[50] Y. Tian, Y. Qiu, X. Hou, L. Wang, G. Liu, Catalytic cracking of JP-10 over HZSM-5 nanosheets, Energy Fuel 31 (2017) 11987–11994.

[51] Y. Tian, B. Zhang, S. Gong, L. Wang, X. Zhang, C. Qiao, G. Liu, Synthesis of pillared nanosheet HZSM-5 zeolite films for catalytic cracking of supercritical n-dodecane, Microporous Mesoporous Mater. 310 (2021), 110598.

[52] J. Hao, D.-g Cheng, F. Chen, X. Zhan, n-Heptane catalytic cracking on ZSM-5 zeolite nanosheets: effect of nanosheet thickness, Microporous Mesoporous Mater. 310 (2021), 110647.

[53] X. Zhang, D. Liu, D. Xu, S. Asahina, K.A. Cychosz, K.V. Agrawal, Y. Al Wahedi, A. Bhan, S. Al Hashimi, O. Terasaki, M. Thommes, M. Tsapatsis, Synthesis of self-pillared zeolite nanosheets by repetitive branching, Science 336 (2012) 1684–1687.

[54] B. Ali, X. Lan, M.T. Arslan, H. Wang, S.Z.A. Gilani, S. Wang, T. Wang, Self-pillared MFI-type zeolite nanosheets as selective catalysts for glycerol dehydration to acrolein, ACS Appl. Nano Mater. 3 (2020) 10966–10977.

[55] L. Ren, Q. Guo, P. Kumar, M. Orazov, D. Xu, S.M. Alhassan, K.A. Mkhoyan, M. E. Davis, M. Tsapatsis, Self-pillared, single-unit-cell Sn-MFI zeolite nanosheets and their use for glucose and lactose isomerization, Angew. Chem. Int. Ed. 54 (2015) 10848–10851.

[56] Y. Tian, H. Liu, L. Wang, X. Zhang, G. Liu, Controllable fabrication and catalytic performance of nanosheet HZSM-5 films by vertical secondary growth, AIChE J. 64 (2018) 1923–1927.

[57] Xinbao Zhu, Xinyu He, Longhui Guo, Yawei Shi, Ning Zhao, Congzhen Qiao, L. Dai, Y. Tian, Hydrophobic modification of ZSM-5-encapsulated uniform Pt nanoparticles for catalytic oxidation of volatile organic compounds, ACS Appl. Nano Mater. 5 (2022) 3374–3385.

[58] J. Pérez-Ramírez, C.H. Christensen, K. Egeblad, C.H. Christensen, J.C. Groen, Hierarchical zeolites: enhanced utilisation of microporous crystals in catalysis by advances in materials design, Chem. Soc. Rev. 37 (2008) 2530–2542.

[59] L. Emdadi, Y. Wu, G. Zhu, C.-C. Chang, W. Fan, T. Pham, R.F. Lobo, D. Liu, Dual template synthesis of meso- and microporous MFI zeolite nanosheet assemblies with tailored activity in catalytic reactions, Chem. Mater. 26 (2014) 1345–1355.

[60] J.M. Escola, J. Aguado, D.P. Serrano, A. García, A. Peral, L. Briones, R. Calvo, E. Fernandez, Catalytic hydroreforming of the polyethylene thermal cracking oil over Ni supported hierarchical zeolites and mesostructured aluminosilicates, Appl. Catal. B: Environ. 106 (2011) 405–415.

[61] C. Chen, J. Zhu, F. Chen, X. Meng, X. Zheng, X. Gao, F.-S. Xiao, Enhanced performance in catalytic combustion of toluene over mesoporous Beta zeolite-supported platinum catalyst, Appl. Catal. B: Environ. 140–141 (2013) 199–205.

[62] K. Mori, T. Itoh, H. Kakudo, T. Iwamoto, Y. Masui, M. Onaka, H. Yamashita, Nickel-supported carbon nitride photocatalyst combined with organic dye for visible-light-driven hydrogen evolution from water, Phys. Chem. Chem. Phys. 17 (2015) 24086–24091.

[63] H. Zhao, X. Hu, J. Hao, N. Li, K. Zhi, R. He, Y. Wang, H. Zhou, Q. Liu, An efficient bifunctional Ru-NbOPO₄ catalyst for the hydrodeoxygenation of aromatic ethers, phenols and real bio-oil, Appl. Catal. A: Gen. 591 (2020), 117378.

[64] H. Vargas-Villagrán, M.A. Flores-Villeda, I. Puente-Lee, D.A. Solís-Casados, A. Gómez-Cortés, G. Díaz-Guerrero, T.E. Klimova, Supported nickel catalysts for anisole hydrodeoxygenation: Increase in the selectivity to cyclohexane, Catal. Today 349 (2020) 26–41.

[65] L. Hu, Z. Chen, W. Sun, T. Cheng, Y. Wei, C. Xu, S. Zhao, Measurement of pore diffusivity in NiMo/Al₂O₃ catalyst pellets by the zero-length column method, Ind. Eng. Chem. Res. 59 (2020) 8426–8435.

[66] L. Guo, Y. Tian, X. He, C. Qiao, G. Liu, Hydrodeoxygenation of phenolics over uniformly dispersed Pt–Ni alloys supported by self–pillared ZSM–5 nanosheets, Fuel 322 (2022), 124082.

[67] M.W. Schreiber, C.P. Plaisance, M. Baumgartl, K. Reuter, A. Jentys, R. Bermejo-Deval, J.A. Lercher, Lewis-Bronsted acid pairs in Ga/H-ZSM-5 to catalyze dehydrogenation of light alkanes, J. Am. Chem. Soc. 140 (2018) 4849–4859.

[68] E.F. Iliopoulou, S.D. Stefanidis, K.G. Kalogiannis, A. Delimitis, A.A. Lappas, K. S. Triantafyllidis, Catalytic upgrading of biomass pyrolysis vapors using transition metal-modified ZSM-5 zeolite, Appl. Catal. B: Environ. 127 (2012) 281–290.

[69] X. He, Y. Tian, L. Guo, C. Qiao, G. Liu, Fabrication of extra–framework Al in ZSM–5 to enhance light olefins production in catalytic cracking of n–pentane, J. Anal. Appl. Pyrolysis 165 (2022), 105550.

[70] S. Schallmoser, T. Ikuno, M.F. Wagenhofer, R. Kolvenbach, G.L. Haller, M. Sanchez-Sanchez, J.A. Lercher, Impact of the local environment of Brønsted

acid sites in ZSM-5 on the catalytic activity in n-pentane cracking, J. Catal. 316 (2014) 93–102.

[71] K. Ebitani, J. Konishi, H. Hattori, Skeletal isomerization of hydrocarbons over zirconium oxide promoted by platinum and sulfate ion, J. Catal. 130 (1991) 257–267.

[72] C.-C. Tran, O. Mohan, A. Banerjee, S.H. Mushrif, S. Kaliaguine, A combined experimental and DFT investigation of selective hydrodeoxygenation of guaiacol over bimetallic carbides, Energy Fuels 34 (2020) 16265–16273.

[73] E.C. Schiesser, E. Blanco, A.B. Dongil, X. Zarate, M. Saavedra-Torres, E. Schott, R. I. Canales, N. Escalona, Insights into hydrodeoxygenation of furfural and guaiacol mixture: experimental and theoretical studies, J. Phys. Chem. C 125 (2021) 7647–7657.